Chinese Chemical Letters 35 (2024) 109066

Contents lists available at ScienceDirect

Chinese Chemical Letters

journal homepage: www.elsevier.com/locate/cclet

Weak interaction-steered evolution of polyoxovanadate-based metal-organic polyhedra from transformation *via* interlock to packing

Yan-Hu Wang[a,1], Ke-Wei Tong[a,1], Chao-Qin Chen[a], Jing Du[b,*], Peng Yang[a,*]

[a] *College of Chemistry and Chemical Engineering, Advanced Catalytic Engineering Research Center of the Ministry of Education, Hunan University, Changsha 410082, China*
[b] *College of Chemistry and Materials Science, Testing and Analysis Center, Hebei Normal University, Shijiazhuang 050024, China*

ARTICLE INFO

Article history:
Received 25 July 2023
Revised 14 August 2023
Accepted 7 September 2023
Available online 9 September 2023

Keywords:
Polyoxometalates
Polyoxovanadates
Metal-organic polyhedron
Interlock
Weak intermolecular forces

ABSTRACT

A bottleneck in biomimetic synthesis consists in the full copy of, for example, the hierarchical structure of proteins directed by weak interactions. By contrast with covalent bonds bearing definite orientation and high stability, weak intermolecular forces within a continuous dynamic equilibrium can be hardly tamed for molecular design. In this endeavor, a ligand-dominated strategy that embodies tunable electrostatic repulsion and $\pi\cdots\pi$ stacking was first employed to shape polyoxovanadate-based metal-organic polyhedra (VMOPs). Structural evolution involving transformation, interlock, and discovery of an unprecedented prototype of the Star of David was hence achievable. Not only as a handy tool for the primary structural control over VMOPs, these weak forces allow for an advanced management on the spatial distribution of such manmade macromolecules as well as the associated physicochemical behaviors, representing an ideal model for simulating and interpreting the conformation-function relationship of proteins.

Weak intermolecular forces (*e.g.*, hydrogen bonds, $\pi\cdots\pi$ stacking, and van der Waals interactions) are vital to master the spatial structure of biomacromolecules as well as their associated functions [1]. Typical examples include the complementary base pairing in DNA and the α-helix/β-sheet in proteins. With the upsurge of biomimetic synthesis, chemists are wild about a higher-order molecular design *via* an ensemble of both covalent bonds and weak forces [2–4]. It is in this context that the research of metal-organic frameworks (MOFs) and metal-organic polyhedra (MOPs) has achieved encouraging progress [5–7]. Thanks to the guidance by reticular chemistry, their fundamental coordination scaffolds are now programmable, on the bench or *in silico* computations, *via* an elaborate combination of secondary building units and organic linkers of various topologies [7,8]. Yet, predictions on the exact structural details are not always reliable as the existence of sophisticated intermolecular weak interactions. It has been established that, along with the ligand extension and resultant enlarged porosity, MOFs prefer to adopt framework interpenetration spontaneously (usually driven by hydrogen bonds and $\pi\cdots\pi$ stacking), in order to get rid of the extra energy that causes metastability [9,10]. In contrast to MOFs of infinite networks, the discrete MOPs apparently suffer a lot more from the weakly interacting constraints inside and outside their cage-like structures [11,12]. Construction of aesthetically pleasing architectures, including distorted and interlocked MOPs are, of course, dominated by coordination interactions, yet the contribution of weak intermolecular forces cannot be ignored [9–12]. As a consequence, it would be challenging and rewarding to understand and take advantage of such weak forces as an effective tool to steer the self-assembly of MOPs.

Amongst MOPs built upon polynuclear metallic vertices, polyoxovanadate-based metal-organic polyhedra (VMOPs), in particular, represent a subset with great developing prospects [13–16]. Facilitated by an atom-by-atom control over both the addenda and heterogroup, the alkoxo-vanadates are capable of being customized into three- (*e.g.*, $[\mathrm{V^{IV}}_6\mathrm{O}_6(\mathrm{OCH}_3)_9(\mathrm{SO}_4)(\mathrm{COO})_3]^{2-}$, $\{\mathrm{V}_6\mathrm{S}\}$) [17], four- (*e.g.*, $[\mathrm{V^{IV}}_4\mathrm{V^{V}}\mathrm{O}_9\mathrm{Cl}(\mathrm{COO})_4]^{2-}$, $\{\mathrm{V}_5\mathrm{Cl}\}$) [18], and five-connected (*e.g.*, $[\mathrm{W^{VI}}\mathrm{V^{IV}}_5\mathrm{O}_{11}(\mathrm{SO}_4)(\mathrm{COO})_5]^{3-}$, $\{\mathrm{V}_5\mathrm{W}\}$) [19] nodes (Fig. S1 in Supporting information). Of these, in combination with a rich reservoir of edge and panel linkers, a large family of Platonic and Archimedean solids have been established with tetrahedral, octahedral, cubic, and spherical configurations [17–29]. In this research frontier, Wang, Su, and Fang *et al.* have greatly advanced the heuristic findings of Hartl [13] and Zaworotko *et al.* [14,30], especially in the structural engineering of modules *via* coordination interactions [17,20–29]. From the research perspective of weak

---

[*] Corresponding authors.
E-mail addresses: duj622@hebtu.edu.cn (J. Du), pengyang216@hnu.edu.cn (P. Yang).
[1] These authors contributed equally to this work.

https://doi.org/10.1016/j.cclet.2023.109066
1001-8417/

forces, on the other side, VMOPs could be considered as viable candidates on account of their tunable charge distribution, adaptive pore size, and distinct template effect. Indeed, the emergence of supramolecular recognition and isomerization in VMOPs delivers a positive signal to exploit the underlying weak interactions in such a system [26,31]. Referenced by the seminal achievements in the related fields of polyoxometalates and molecular cages, weak intermolecular forces are nowadays valued for shaping high-nuclear clusters [32], as well as for directing the steric configuration of manmade macromolecules [33–44], which are of central importance in biological modeling synthesis.

Adoption of a ligand-dominated strategy that embodies tunable electrostatic repulsion and $\pi\cdots\pi$ stacking, we attempted to tap the potential of such weak forces on the structural regulation of VMOPs. In our work, a series of dipolar ligands with varied lengths and angles were pre-synthesized to scaffold VMOPs towards a metastable state, which would set the stage for watching the possible weak interactions formed spontaneously. In addition to evaluating their type and strength, such forces were hired for a multi-scale structural design from basic geometry *via* bimolecular interlock to spatial packing, in a manner analogous to the hierarchical proteins evolved in nature.

By means of one-pot reactions under solvothermal conditions, a group of five linear dicarboxylic ligands that vary in length, namely H_2AzDC (azobenzene-4,4′-dicarboxylic acid), H_2EDC (4,4′-ethynylenedibenzoic acid), H_2TPDC ([*p*-terphenyl]−4,4′′-dicarboxylic acid), H_2QPDC ([1,1′:4′,1′′:4′′,1′′′-quaterphenyl]−4,4′′′-dicarboxylic acid), H_2PEBDC {(4,4′-(1,4-phenylenebis(ethyne-2,1-diyl))dibenzoic acid)}, were selected to assemble with the *in-situ* formed {V_6S} for building VMOPs of the supposed tetrahedral archetype (see Supporting information). Beyond our expectation, the tetramethylammonium (TMA) salts of three anticipated "tetrahedra" (VMOTs) and two unprecedented "capsules" (VMOCs) were obtained respectively:

$(TMA)_8\{[V_6O_6(OCH_3)_9(SO_4)]_4(AzDC)_6\}\cdot16CH_3OH\cdot15DMF$ (**TMA-VMOT-1**);

$(TMA)_8\{[V_6O_6(OCH_3)_9(SO_4)]_4(EDC)_6\}\cdot xCH_3OH\cdot yDMF$ (**TMA-VMOT-2**) [31];

$(TMA)_8\{[V_6O_6(OCH_3)_9(SO_4)]_4(TPDC)_6\}\cdot17CH_3OH\cdot11DMF$ (**TMA-VMOT-3**);

$(TMA)_4\{[V_6O_6(OCH_3)_9(SO_4)]_2(QPDC)_3\}\cdot3CH_3OH\cdot3DMF$ (**TMA-VMOC-4**);

$(TMA)_4\{[V_6O_6(OCH_3)_9(SO_4)]_2(PEBDC)_3\}\cdot13CH_3OH\cdot13DMF$ (**TMA-VMOC-5**).

In general, the applied ligand-elongation strategy could largely vary the pore size but not the topology of backbones, as previously indicated in the study of IRMOFs [45]. As expected, two regular tetrahedra of **VMOT-1** and **VMOT-2** were received using AzDC and EDC as respective linkers. In a typical tetrahedral geometry, four {V_6S} motifs serving as three-connected vertices are bridged by six organic ligands as edges, of which the length fall into the range of 13.0–13.6 Å (Figs. 1a and b). If displacing the linker with a prolonged TPDC (15.7 Å), a concave tetrahedron of **VMOT-3** was obtained (Fig. 1c). It has been noted that the six edges bend inwards the body center, resulting in curves with an average radian of 0.14 π (Fig. S2a in Supporting information). Further elongation of the ligands to QPDC (20.0 Å) and PEBDC (20.7 Å) led to a drastic conversion from the classical tetrahedron to an unprecedented capsule-style cage. In the structure of **VMOC-4** and **VMOC-5**, two {V_6S} units occupy the two poles and are vertically bridged by three ligands, with an idealized point group symmetry of D_{3h} (Figs. 1d and e). On the contrary to the bending mode in **VMOT-**

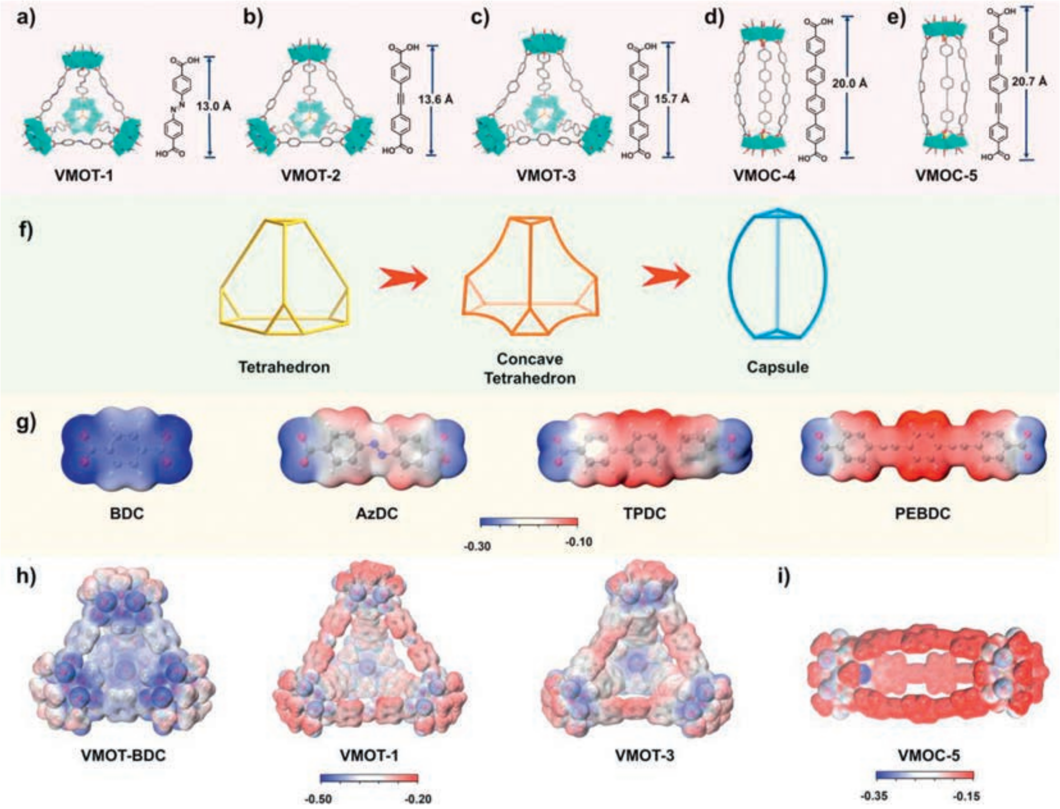

Fig. 1. Transformation steered by ligand extension of varied electrostatic potential. (a-e) Combined polyhedral/stick representation of **VMOT-1∼3**, **VMOC-4**, and **VMOC-5**. Color code: {VO_6}, turquoise octahedra; S, yellow; O, red; N, blue; C, gray. Hydrogen atoms are omitted for clarity. (f) Structural evolution from tetrahedron (**VMOT-1** and **VMOT-2**) *via* a concave intermediate (**VMOT-3**) to capsule (**VMOC-4** and **VMOC-5**). (g) Electrostatic potential map (isovalue 0.01) of the representative ligands, and (h) of the corresponding **VMOT-BDC**, **VMOT-1**, **VMOT-3**, as well as (i) **VMOC-5**. Blue: electron accumulation; red: electron depletion.

3, the edges herein bulge outwards in the middle with an average radian of 0.24 π (**VMOC-4**) and 0.18 π (**VMOC-5**), respectively (Figs. S2b and c in Supporting information). It follows from the above that a rare structural evolution of VMOPs, from tetrahedron *via* a concave intermediate to capsule, was achieved as a function of ligand length (Fig. 1f). To explain this from the standpoint of weak interactions, a systematic analysis on their electrostatic potential (ESP) diagrams was carried out [46].

As depicted in Fig. 1g, the ESP of several representative dicarboxylic acid-based ligands were calculated. From the perspective of electric potential distribution, the more negative ESP values are predominantly located on the carboxylic functions, while the ESP values in the middle of the ligands are relatively positive. As the length of ligands being extended from BDC (terephthalate) to PEBDC, the nucleophilicity of the central aromatic parts decreases correspondingly. So, a progressive separation of ESP was clearly evidenced in the linear ligands being used. As shown in Fig. 1h, the ESP surfaces of VMOT regions are primarily concentrated on the semi-exposed sulfate heterogroups. Therefore, it is speculated that the electrostatic repulsion between the sulfate functions and peripheral aromatic domains is essential for supporting the tetrahedral configuration. From the referenced **VMOT-BDC** ($\{[V_6O_6(OCH_3)_9(SO_4)]_4(BDC)_6\}$, Fig. S3a in Supporting information) [17] to **VMOT-3**, such repulsive forces are gradually weakened till the formation of a pressure-bearing concave state with inadequate inner support. Upon further stretch of the edges, the assumed tetrahedra might become unstable and be forced to shrink into a compact capsule-like archetype (Fig. 1i). Accordingly, the opening angles in the three-connected $\{V_6S\}$ are shifted from a diverging pattern (*e.g.*, $\theta = 29.5°$ in **VMOT-1**, Table S1 in Supporting information) to a convergent fashion (*e.g.*, $\theta = 12.0°$ in **VMOC-5**), in an effort to gather the ligands and restore the internal electrostatic forces. As demonstrated by the thermogravimetric analysis, the decomposition of **TMA-VMOT-1** and **TMA-VMOC-4** was ended at ≥ 500 °C (Figs. S4a and b in Supporting information), while **TMA-VMOT-3** was completely destructed at a lower temperature (468 °C, Fig. S4c in Supporting information), testifying its metastability from another view.

Inspired by these findings, it interested us more to verify whether such electrostatic forces are able to steer the structural transformation on purpose. Previous research has experienced the deformation of VMOPs *via* the substitution of sulfate ($\{V_6S\}$) by a sterically demanding phenylphosphate ($\{V_6P\}$) within a confined space [27–29]. Different from the above, the void in **VMOT-1~3** are large enough to ignore the steric hindrance of heterogroups, while the distribution of ESP on $\{V_6P\}$ should be varied. In this way, the replacement of $\{V_6S\} \rightarrow \{V_6P\}$ was proceeded in the scenario of as-made compounds. Of prime interest, the original tetrahedra of **VMOT-1~3** were converted into their respective capsule-style counterparts **VMOC-P-1~3** (Figs. 2a–c). Besides, the backbone of the derived **VMOC-P-4** and **VMOC-P-5** remain nearly unchanged (Figs. 2d and e). The formula of their TMA salts are listed below:

$(TMA)_4\{[V_6O_6(OCH_3)_9(PhPO_3)]_2(AzDC)_3\}\cdot6CH_3OH\cdot3DMF$ (**TMA-VMOC-P-1**);

$(TMA)_4\{[V_6O_6(OCH_3)_9(PhPO_3)]_2(EDC)_3\}\cdot7CH_3OH\cdot5DMF$ (**TMA-VMOC-P-2**);

$(TMA)_4\{[V_6O_6(OCH_3)_9(PhPO_3)]_2(TPDC)_3\}\cdot11CH_3OH\cdot7DMF$ (**TMA-VMOC-P-3**);

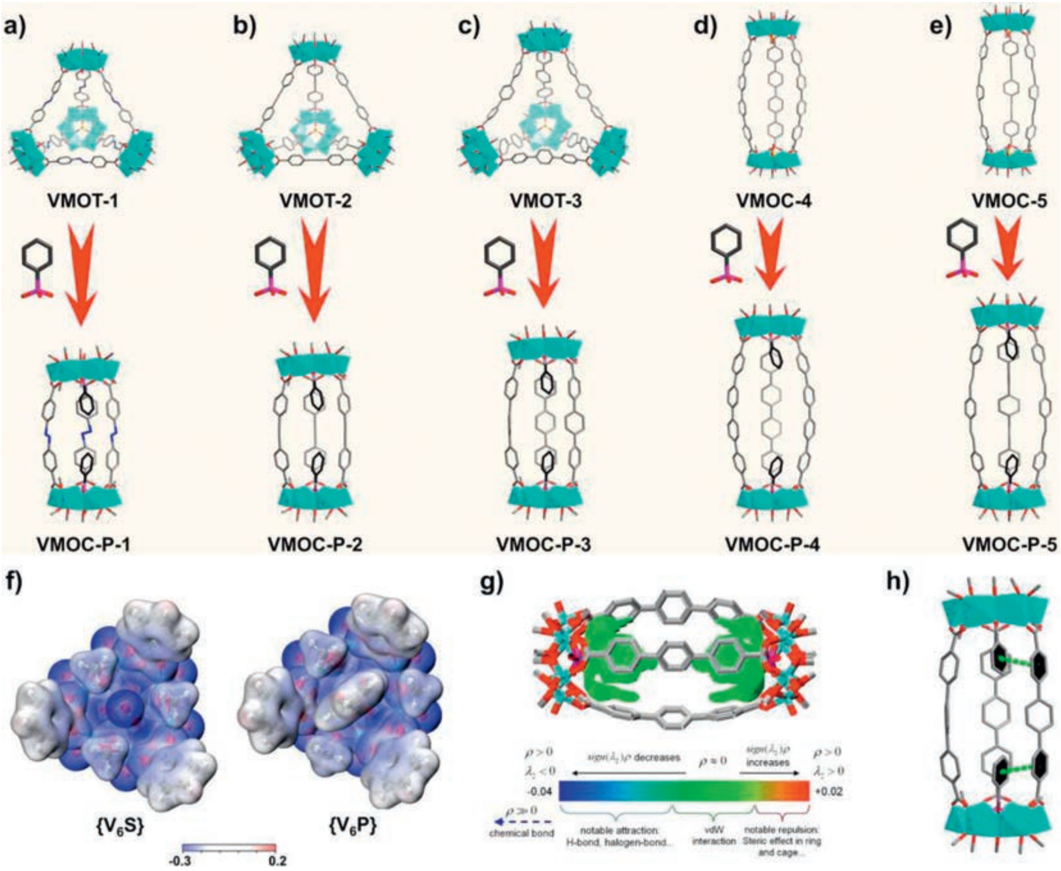

Fig. 2. Transformation steered by vertice replacement of tunable electrostatic potential and IGMH analyses. (a–c) Structural transformation from the tetrahedral (**VMOT-1~3**) to capsule-like archetype (**VMOC-P-1~3**) *via* vertice replacement. (d, e) Vertice exchange from **VMOC-4** and **VMOC-5** to **VMOC-P-4** and **VMOC-P-5**. (f) Electrostatic potential map (isovalue 0.01) of $\{V_6S\}$ and $\{V_6P\}$. (g) The $sign(\lambda_2)\rho$ colored isosurfaces of $\delta g^{inter} = 0.001$ a.u. of **VMOC-P-3** corresponding to IGMH analyses (The color bar represents the common interpretation of coloring method of mapped function $sign(\lambda_2)\rho$ in IGMH maps). (h) The $\pi \cdots \pi$ interactions (dotted green line) in **VMOC-P-3**.

$(TMA)_4\{[V_6O_6(OCH_3)_9(PhPO_3)]_2(QPDC)_3\}\cdot 3CH_3OH\cdot 4DMF$ (**TMA-VMOC-P-4**);
$(TMA)_4\{[V_6O_6(OCH_3)_9(PhPO_3)]_2(PEBDC)_3\}\cdot 3CH_3OH\cdot 5DMF$ (**TMA-VMOC-P-5**).

Apparently, the ESP analysis showcased a reduced nucleophilicity on the heterogroup after the exchange of $\{V_6S\}\rightarrow\{V_6P\}$ (Fig. 2f). As a result, the electrostatic repulsion in the cage could be further turned down, thereby aiding the conversion from tetrahedron (**VMOT-1~3**) to capsule (**VMOC-P-1~3**), which is in full agreement with the experimental data. It should also be stressed that, in the previous study on vertice replacement, the tetrahedral backbone with relatively short edges are maintained in **VMOT-P-BDC** ($\{[V_6O_6(OCH_3)_9(PhPO_3)]_4(BDC)_6\}$, Figs. S3b and c in Supporting information) and **VMOT-P-NDC** ($\{[V_6O_6(OCH_3)_9(PhPO_3)]_4(NDC)_6\}$, NDC = naphthalene-2,6-dicarboxylate, Fig. S3d in Supporting information) [27,47]. Thus it can be seen that, a manual switch of configuration is accessible in VMOPs on condition of prolonged linkers being used. By virtue of the regulation on the difference of ESP either on the edge or vertice, the processable weak electrostatic repulsion could assume more responsibility for the structural engineering of such macromolecules. To visualize the region of non-covalent interactions within **VMOC-P-3**, we applied the independent gradient model based on the Hirshfeld partition (IGMH) method [48] to process the calculated electron densities in the Multiwfn code [49]. The van der Waals interactions were colored by green and imaged with a Visual Molecular Dynamics (VMD) 1.9.3 software [50]. From the IGMH map (Fig. 2g), it can be seen that a thin and broad isosurface appears between the phenyl group in $\{V_6P\}$ and nearby aromatic linkers, which ideally exhibits $\pi\cdots\pi$ and C–H$\cdots\pi$ interactions. Through the substitution of $\{V_6S\}\rightarrow\{V_6P\}$, additional van der Waals interactions could be generated between the vertices and linkers, which would further weaken the repulsion between them and hence in favor of a capsule-like architecture. A lower and more-stable energy state after the structural transformation was again proved by thermogravimetric analysis. As exemplified by **TMA-VMOT-3** → **TMA-VMOC-P-3**, the final decomposition temperature was markedly increased from 468 °C to 501 °C (Fig. S4d in Supporting information). Meanwhile, the emergence of $\pi\cdots\pi$ stacking was also defined in the crystal structure of all $\{V_6P\}$-based capsules (*e.g.*, centroid-to-centroid distance of 3.92 Å in **VMOC-P-3**, Fig. 2h), reminding us to exam the $\pi\cdots\pi$ interactions appeared in the whole system.

A detailed review on the structure of **VMOT-3** disclosed a face-directed interlock of two concave tetrahedra, resulting in a shuttle-shaped supramolecular assembly (Figs. 3a and b). Of the two pieces being interpenetrated, one is flipped over 180° and then hooked with the other on the central belt. The view from the top pictures a hexagram made up of two stagger basal planes, which are glued by six groups of $\pi\cdots\pi$ stacking (Fig. 3c). Specifically, the phenyl rings in the middle of the three linkers (purple) adopt face-to-face interactions with the corresponding aromatic groups next to the vertices (brown), with the centroid-to-centroid distances ranging from 3.76 Å to 3.91 Å. Based on the semi-stable tetrahedron of **VMOT-3**, the presence of bimolecular interpenetration is understandable as to spontaneously fill the large pores and improve their mutual stability. Being calculated by the Multiwfn code [48] using the Bondi van der Waals radius [51], the pore volume in **VMOT-3** is compressed from 1337.98 Å^3 (individual) to 635.63 Å^3 (interlocked), almost halving the central space (Fig. S5 in Supporting information). Fig. 3d presents the $sign(\lambda_2)\rho$ colored IGMH δ_g^{inter} isosurfaces of 0.001 a.u., the two individual tetrahedra are respectively defined as separate fragments. Notably, evident $\pi\cdots\pi$ interactions are positioned in the middle aromatic area of ligands, as there exists a flat and broad δ_g^{inter} isosurface. It is apparent that, with the increasing number of aromatic groups, the ESP distribution in the middle of the linkers would be weakened, whereas the intermolecular $\pi\cdots\pi$ interactions get strengthened instead, which jointly power the interpenetration of such tetrahedra. As another kind of weak forces found in the VMOP system, the role of $\pi\cdots\pi$

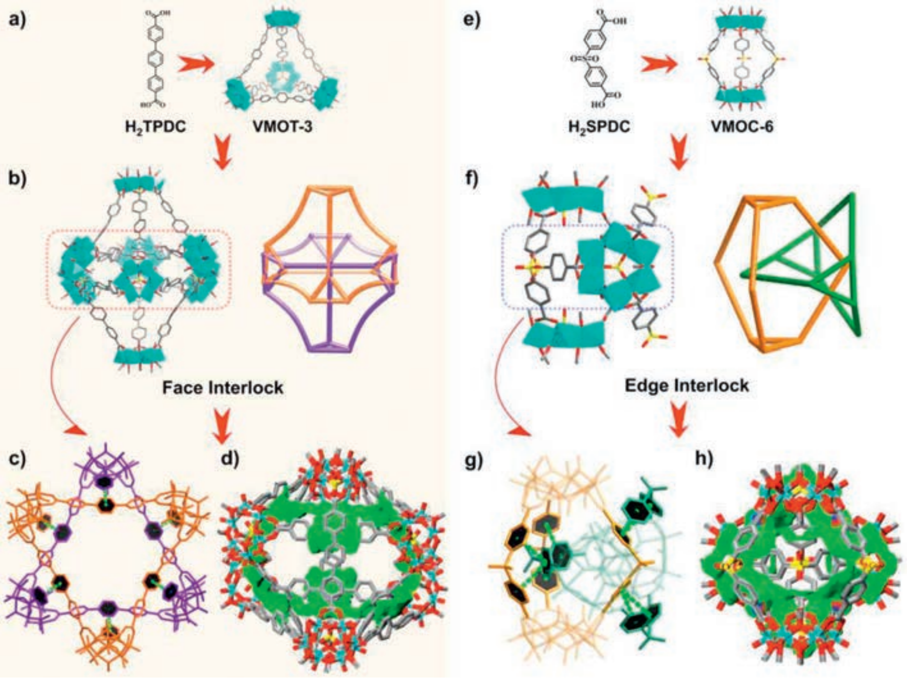

Fig. 3. Structural and IGMH analyses of the face- and edge-interlock assembly. Structural representation of (a) the individual **VMOT-3** and (b) its bimolecular face-interlock assembly. (c) The $\pi\cdots\pi$ interactions in the face-interlock assembly of **VMOT-3**. (d) The $sign(\lambda_2)\rho$ colored isosurfaces of $\delta_g^{inter} = 0.001$ a.u. corresponding to IGMH analyses for the face-interlock assembly of **VMOT-3**. Structural representation of e) the individual **VMOC-6** and (f) its bimolecular edge-interlock assembly. (g) The $\pi\cdots\pi$ interactions in the edge-interlock assembly of **VMOC-6**. (h) The $sign(\lambda_2)\rho$ colored isosurfaces of $\delta_g^{inter} = 0.0005$ a.u. corresponding to IGMH analyses for the edge-interlock assembly of **VMOC-6**.

stacking in the management of bimolecular aggregation states deserves further investigation.

In an effort to introduce $\pi\cdots\pi$ stacking into the family of VMOCs, H_2SPDC (4,4′-sulfonyldibenzoic acid) was employed as linker with a flexible dihedral angle. Considering the electron-withdrawing sulfonyl group in the middle of the edge (*i.e.*, reduced nucleophilicity on the aromatic area, Fig. S6 in Supporting information), a capsule-like cage was envisioned initially because of the relatively weak electrostatic repulsion within it. Moreover, the central void in the prospective capsule might be enlarged due to the folding nature of edges, thereby creating favorable conditions for $\pi\cdots\pi$ interactions. As expected, a capsule with the formula $(TMA)_4\{[V_6O_6(OMe)_9(SO_4)]_2(SPDC)_3\}\cdot 6CH_3OH\cdot 5DMF$ (**TMA-VMOC-6**) was harvested successfully. In the structure of **VMOC-6**, the three edges display a bulgy configuration with the dihedral angles fall in the range of 106.00° to 113.23°, making room for a larger interior space (Fig. 3e). In order to liberate the excess energy, two of such capsules are cross-linked perpendicularly to afford an edge-interlock mode, which is stabilized by four sets of $\pi\cdots\pi$ interactions (Fig. 3f). For each **VMOC-6**, the edge being entangled penetrates into the domain that is enclosed by two non-locked linkers of the other cage. Every aromatic ring of the former interacts with the two phenyls of the latter, with an average centroid-to-centroid distance of 4.20 Å (Fig. 3g). As illustrated in Fig. 3h, the IGMH analyses showcased the interactions of $\pi\cdots\pi$ stacking are mainly concentrated in the center of the dimer, and are much enhanced compared to that in the face-interlock **VMOT-3**. This tells us that, by adjusting the folding angle of edges, additional sites for $\pi\cdots\pi$ interactions inside the capsule would be provided, giving rise to a tighter interlocked pattern of narrow space (65.66 Å^3, Fig. S7 in Supporting information). From the above, it is confirmed that $\pi\cdots\pi$ stacking could be engaged to customize the mechanically interlocked VMOPs of varying archetypes, thereby broadening the scope of design from individual molecule to supramolecular aggregates.

What if the two weak forces are simultaneously amplified in one system? In other words, a synergistic strategy of ligand stretch and vertice replacement was taken to severely weaken the electrostatic repulsion. At the same time, expanding further the central cavity to maximize the satisfaction of $\pi\cdots\pi$ stacking and framework interpenetration. To meet these requirements, a customized ligand of H_2DBIDC (1,4-bis(5-carboxy-1*H*-benzimidazole-2-yl) benzene) was involved in the synthesis, and a "hexagram"-like prototype (Fig. 4a) was obtained for the first time: $(TMA)_{12}\{[V_6O_6(OCH_3)_9(PhPO_3)]_6(DBIDC)_9\}\cdot 40CH_3OH\cdot 15DMF$ (**TMA-VMOH-P-1**).

In view of the prolonged linker (19.0 Å) and $\{V_6P\}$ vertice of reduced nucleophilicity, a capsule-like cage could be foreseen (Fig. S8 in Supporting information). However, the V-shaped coordination of DBIDC significantly distorts the pristine capsule, and finally breaks it from one side. Then the two arms being thrown out are united with another $\{V_6P\}$ to re-form a basket-like assembly (Fig. 4b). The remained connection point on the handle of each basket are occupied by a shared Z-shaped DBIDC, which pierces through the subface of both and bounds them together. It is obvious that the open basket encompasses a larger nanoscale central void, wherein the distance from the bottom center to apex (the outmost carbon atom in $\{V_6P\}$) is 15.58 Å (Fig. S9 in Supporting information). In

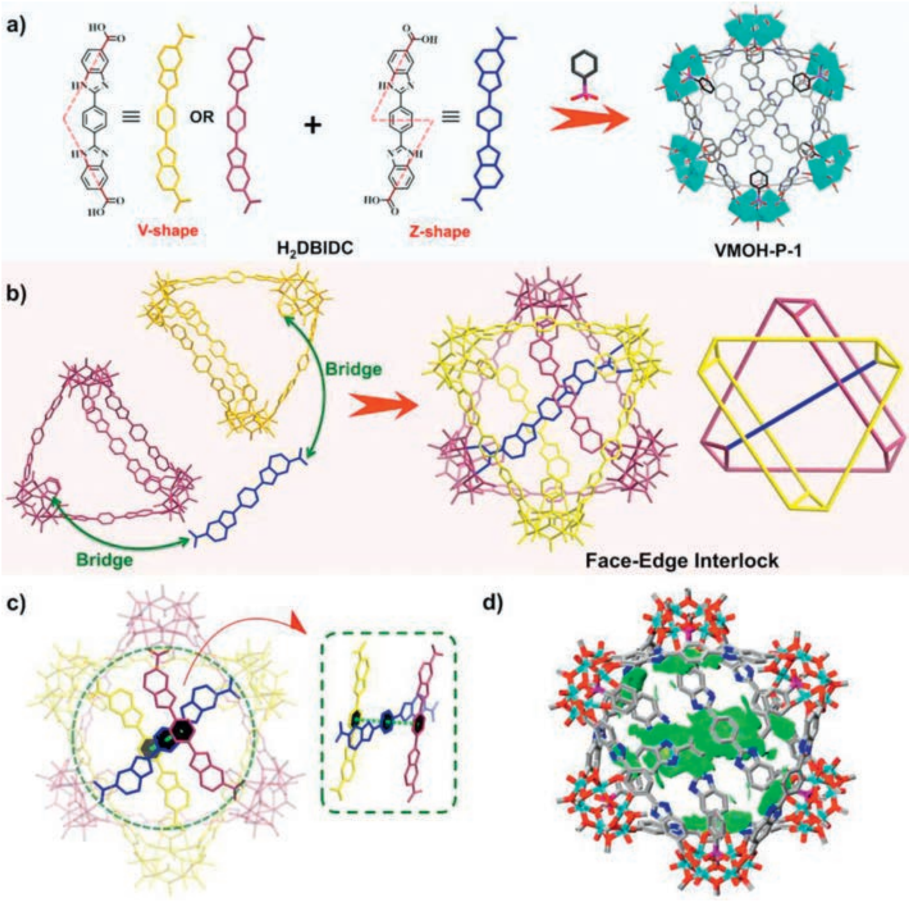

Fig. 4. Structural and IGMH analyses of the Star of David. (a) The assembly process of VMOH-P-1. (b) The face-edge-interlock mode in VMOH-P-1. (c) The $\pi\cdots\pi$ interactions in VMOH-P-1. (d) The $sign(\lambda_2)\rho$ colored isosurfaces of $\delta_g^{inter} = 0.001$ a.u. corresponding to IGMH analyses for VMOH-P-1.

this context, a mixed face-edge-interlock pattern directed by $\pi\cdots\pi$ stacking was generated. In the center of **VMOH-P-1**, two sets of face-to-face aromatic interactions are located, with the centroid-to-centroid distance of 3.80 Å (Fig. 4c). According to the IGMH analyses shown in Fig. 4d, installation of aromatic groups on both the vertices and edges would make for more intense intramolecular weak interactions presented in **VMOH-P-1**. From the $\delta_g{}^{\text{inter}}$ isosurface, in addition to the identified $\pi\cdots\pi$ stacking amongst the linkers in the center, the C–H$\cdots\pi$ interactions appear as well between the ligands and heterogroups around vertices. It is certain that a modification on both the ligand and vertice would promote the communication of weak forces within **VMOH-P-1**, and further orchestrate the face- and edge-interlock modes in one system. As all said above, the integration of both electrostatic repulsion and $\pi\cdots\pi$ stacking is full of unlimited potential, especially in the development of spectacular architectures beyond the classical polyhedra of high symmetries.

To deepen our understanding in the weak interaction-steered VMOPs, the research focus was moved from the primary structures towards their distribution in the three-dimensional (3D) space. On top of this is disclosure of the relationship between the molecular spatial arrangement and associated physicochemical properties. Directed by electrostatic repulsion and $\pi\cdots\pi$ stacking, the evolution of VMOPs is reflected not only in their structural types but also the adjustable electronegativity. From capsule *via* tetrahedron to hexagram, the stoichiometric ratio of vertices *VS* linkers are 2:3, 4:6, and 6:9, respectively, corresponding to a gradually enhanced negative charge of −4, −8, and −12. Herein, the {V_6P}-based capsule (**TMA-VMOC-P-2**), tetrahedron (**TMA-VMOT-P-NDC**), and hexagram (**TMA-VMOH-P-1**) were selected for dye adsorption. Similar to the behavior of reported VMOPs [22,26,28,47], **TMA-VMOC-P-2** (Fig. 5a), **TMA-VMOT-P-NDC** (Fig. 5b), and **TMA-VMOH-P-1** (Fig. 5c) exclusively adsorbed the cationic MB^+ (methylene blue) rather than the neutral SD^0 (Sudan I, Fig. S10 in Supporting information) or anionic AO^- (acid orange, Fig. S11 in Supporting information). It was noted that VMOPs bearing higher negative charges (**VMOH-P-1** > **VMOT-P-NDC** > **VMOC-P-2**) behaved a faster adsorption rate and larger loading capacity (Fig. 5d), which could be attributed to the cation-exchange mechanism between MB^+ and TMA^+ molecules.

It is noteworthy that the equally charged capsules in **TMA-VMOC-P-1∼5**, on the other hand, adopt two types of packing modes. Along with the ligand extension from AzDC to PEBDC the corresponding radian of edges gradually increases from 0.12 π to 0.20 π (Figs. S12–S14 in Supporting information). For **TMA-VMOC-P-1∼3**, the neighboring capsules are ordered by two or three sets of $\pi\cdots\pi$ stacking (*e.g.*, centroid-to-centroid distance of 4.15 Å in **TMA-VMOC-P-2**), and are further cascaded into a wave-like 1D chain. Such chains are packed in parallel with each other, resulting in a supramolecular network with zigzag channels (Fig. 5e). By sharp contrast, in the spatial arrangement of **TMA-VMOC-P-4** and **TMA-VMOC-P-5**, their significantly bulgy edges might exert additional steric constraints to diminish the probability of $\pi\cdots\pi$ interactions amongst themselves. As a result, the adjacent capsules are arranged above and below the same layer alternatively, and a honeycomb-like framework with hexagonal channels was achieved

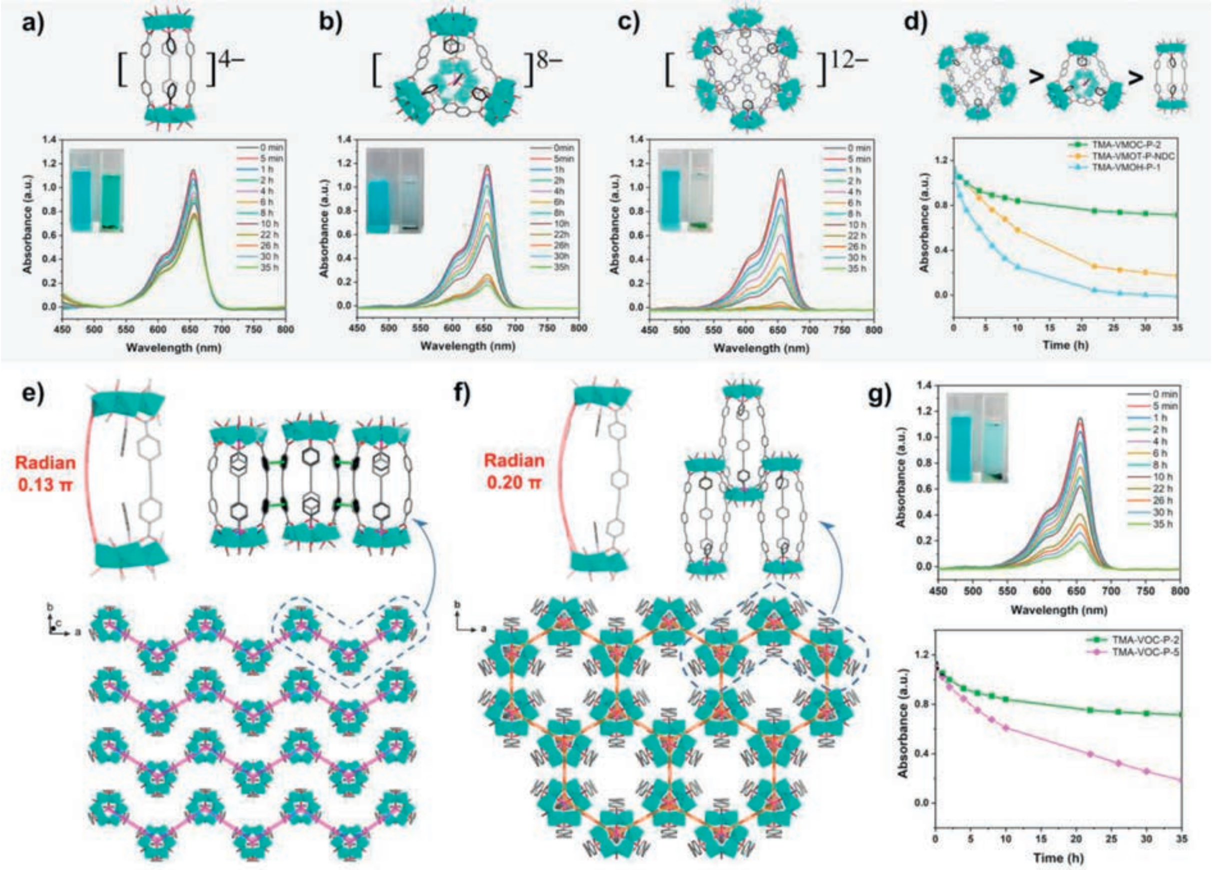

Fig. 5. Relationship of spatial packing and dye adsorption performance. (a-c) The UV–vis spectra of MB^+ in ethanol in the presence of **TMA-VMOC-P-2**, **TMA-VMOT-P-NDC**, and **TMA-VMOH-P-1** at various time intervals (inset, photographs of the color of dye solutions before and after adsorption). (d) The comparison of adsorption performance of selected VMOPs. (e) The crystal packing diagram of **TMA-VMOC-P-2** ordered by $\pi\cdots\pi$ stacking. (f) The crystal packing diagram of **TMA-VMOC-P-5** without $\pi\cdots\pi$ interactions. (g) The UV–vis spectra of MB^+ in ethanol in the presence of **TMA-VMOC-P-5** at various time intervals, as well as the adsorption performance compared to that of **TMA-VMOC-P-2**.

instead (Fig. 5f). Interestingly, a better adsorption performance of **TMA-VMOC-P-5** was reached as compared to that of **TMA-VMOC-P-2** (Fig. 5g), albeit the channels in both are large enough to store MB^+ molecules. One possible explanation for this may be the distinct microenvironment for $\pi \cdots \pi$ interactions between the capsule and MB^+ molecules. Since most of the aromatic groups are taken up for the $\pi \cdots \pi$ stacking of capsules in between, MB^+ are unlikely to enter the channels in **TMA-VMOC-P-2** without appropriate binding sites (Fig. S15 in Supporting information). In **TMA-VMOC-P-5**, however, the three aromatic linkers are all free and face to the center of the hexagons, which is propitious to accommodate MB^+ *via* $\pi \cdots \pi$ interactions (Fig. S16 in Supporting information). From the above, weak intermolecular forces can be taken as chemist's right hand to challenge the spatial control over macromolecules of higher difficulty. Therefore, the weak force-directed VMOPs are on the right track for a complete simulation of protein's multi-level structures, as well as the associated conformation-function relationship.

In response to ligand design, the spontaneous electrostatic repulsion and $\pi \cdots \pi$ stacking were magnified and captured together with the structural evolution of VMOPs. These weak interactions were, in turn, hired to direct the structural transformation, interlock, and even to develop a Star-of-David prototype of VMOPs, either alone or in collaboration. But more than that was the successful customization on the packing mode has been proved to be competent for a protein-mimicking, hierarchical management on the self-assembly of VMOPs, from coordination framework geometries *via* bimolecular aggregation states to spatial distribution characteristics. Our work promises a feasible route for the design of VMOPs by electrostatic repulsion and $\pi \cdots \pi$ stacking, in addition to the conventional modular matching. Also, being dramatically responsive to the weak intermolecular forces, such a system represents an ideal model for simulating and elucidating the conformation-function mechanism in proteins at a molecular scale.

Declaration of competing interest

The authors declare that they have no known competing financial interests or personal relationships that could have appeared to influence the work reported in this paper.

Acknowledgments

This research was financially supported by the National Natural Science Foundation of China (No. 22001066), the Natural Science Foundation of Hunan Province (Nos. 2021JJ40049 and 2022JJ20007), and the Science and Technology Innovation Program of Hunan Province (No. 2022RC1115). J. Du acknowledges the Science and Technology Project of Hebei Education Department (No. QN2023049), Science Foundation of Hebei Normal University (No. L2023B51), and TianHe-2 (LvLiang, China) Cloud Computing Center for support.

Supplementary materials

Supplementary material associated with this article can be found, in the online version, at doi:10.1016/j.cclet.2023.109066.

References

[1] S. Garcia-Manyes, A.E.M. Beedle, Nat. Rev. Chem. 1 (2017) 0083.
[2] C.S.S.R. Kumar, Biomimetic and Bioinspired Nanomaterials, Wiey-VCH Verlag GmbH & Co KGaA, Weinheim, 2010, p. 564.
[3] V. Kulikov, N.A.B. Johnson, A.J. Surman, et al., Angew. Chem. Int. Ed. 56 (2017) 1141–1145.
[4] J.H. Deng, J. Luo, Y.L. Mao, et al., Sci. Adv. 6 (2020) eaax9976.
[5] V. Guillerm, D. Kim, J.F. Eubank, et al., Chem. Soc. Rev. 43 (2014) 6141–6172.
[6] S. Lee, H. Jeong, D. Nam, M.S. Lah, W. Choe, Chem. Soc. Rev. 50 (2021) 528–555.
[7] A. Kondinski, A. Menon, D. Nurkowski, et al., J. Am. Chem. Soc. 144 (2022) 11713–11728.
[8] S.J. Lyle, R.W. Flaig, K.E. Cordova, O.M. Yaghi, J. Chem. Educ. 95 (2018) 1512–1519.
[9] R. Zhu, J. Ding, L. Jin, H. Pang, Coord. Chem. Rev. 389 (2019) 119–140.
[10] J. Hao, F. Lang, L. Hao, et al., Chin. Chem. Lett. (2023) 108310.
[11] A.J. Gosselin, C.A. Rowland, E.D. Bloch, Chem. Rev. 120 (2020) 8987–9014.
[12] G.L. Li, Z. Zhuo, B. Wang, et al., J. Am. Chem. Soc. 143 (2021) 10920–10929.
[13] J. Spandl, I. Brüdgam, H. Hartl, Angew. Chem. Int. Ed. 40 (2001) 4018–4020.
[14] Z. Zhang, L. Wojtas, M.J. Zaworotko, Chem. Sci. 5 (2014) 927–931.
[15] A.W. Augustyniak, M. Fandzloch, M. Domingo, I. Łakomskab, J.A.R. Navarro, Chem. Commun. 51 (2015) 14724–14727.
[16] X.X. Li, D. Zhao, S.T. Zheng, Coord. Chem. Rev. 397 (2019) 220–240.
[17] Y.T. Zhang, X.L. Wang, S.B. Li, et al., Chem. Commun. 52 (2016) 9632–9635.
[18] G.B. Karet, Z. Sun, D.D. Heinrich, et al., Inorg. Chem. 35 (1996) 6450–6460.
[19] Y. Zhang, H. Gan, C. Qin, et al., J. Am. Chem. Soc. 140 (2018) 17365–17368.
[20] Y.T. Zhang, X.L. Wang, E.L. Zhou, et al., Dalton Trans. 45 (2016) 3698–3701.
[21] Y. Zhang, X. Wang, S. Li, et al., Inorg. Chem. 55 (2016) 8770–8775.
[22] Y.R. Gong, W.C. Chen, L. Zhao, et al., Dalton Trans. 47 (2018) 12979–12983.
[23] N. Xu, H. Gan, C. Qin, X. Wang, Z. Su, Angew. Chem. Int. Ed. 58 (2019) 4649–4653.
[24] Y. Gong, Y. Tao, N. Xu, et al., Chem. Commun. 55 (2019) 10701–10704.
[25] Y. Gong, C. Qin, Y. Zhang, et al., Angew. Chem. Int. Ed. 59 (2020) 22034–22038.
[26] H. Gan, N. Xu, C. Qin, et al., Nat. Commun. 11 (2020) 4103–4110.
[27] J. Guo, Q. Chang, Z. Liu, et al., Chem. Sci. 12 (2021) 7361–7368.
[28] J. Guo, J. Liu, Y. Cui, et al., Chem. Sci. 13 (2022) 5718–5725.
[29] Y. Yang, Y. Fu, S. Wu, et al., Inorg. Chem. 62 (2023) 648–652.
[30] Z. Zhang, W.Y. Gao, L. Wojtas, Z. Zhang, M.J. Zaworotko, Chem. Commun. 51 (2015) 9223–9226.
[31] Y. Gong, Y. Zhang, C. Qin, et al., Angew. Chem. Int. Ed. 58 (2019) 780–784.
[32] M. Zhu, S. Han, J. Liu, et al., Angew. Chem. Int. Ed. 61 (2022) e202213910.
[33] Q. Gu, X.L. Zhao, M. Meng, et al., Chin. Chem. Lett. 34 (2023) 107444.
[34] M. Frank, M.D. Johnstone, G.H. Clever, Chem. Eur. J. 22 (2016) 14104–14125.
[35] M. Pan, K. Wu, J.H. Zhang, C.Y. Su, Coord. Chem. Rev. 378 (2019) 333–349.
[36] D. Zang, H. Wang, Polyoxometalates 1 (2022) 9140006.
[37] H. Zhang, W.L. Zhao, H. Li, et al., Polyoxometalates 1 (2022) 9140011.
[38] D. Zang, X.J. Gao, L. Li, Y. Wei, H. Wang, Nano Res. 15 (2022) 8872–8879.
[39] D. Zang, Q. Li, G. Dai, et al., Appl. Catal. B 281 (2021) 119426.
[40] J.H. Ding, Y.F. Liu, Z.T. Tian, et al., Inorg. Chem. Front. 10 (2023) 3195–3201.
[41] K. Qin, D. Zang, Y. Wei, Chin. Chem. Lett. 34 (2023) 107999.
[42] L.M. Wang, W.Y. Liu, M.L. Hu, et al., Rare Met. 41 (2022) 2701–2710.
[43] X. Huang, W. Cui, S. Liu, et al., Chin. Chem. Lett. 34 (2023) 107692.
[44] X. Huang, S. Liu, G. Liu, et al., Appl. Catal. B 323 (2023) 122134.
[45] M. Eddaoudi, J. Kim, N. Rosi, et al., Science 295 (2022) 469–472.
[46] R. Gao, Z. Liu, Z. Liu, et al., Angew. Chem. Int. Ed. 62 (2023) e202300151.
[47] Y. Hou, H. Chen, T. Zhang, et al., J. Coord. Chem. 75 (2022) 1781–1790.
[48] T. Lu, Q. Chen, J. Comput. Chem. 43 (2022) 539–555.
[49] T. Lu, F. Chen, J. Comput. Chem. 33 (2012) 580–592.
[50] W. Humphrey, A. Dalke, K. Schulten, J. Mol. Graph. Model. 14 (1996) 33–38.
[51] A. Bondi, J. Phys. Chem. 68 (1964) 441–451.